Chemical Engineering Journal 505 (2025) 159326

Contents lists available at ScienceDirect

Chemical Engineering Journal

journal homepage: www.elsevier.com/locate/cej

Ultrafast thermal shock synthesis of nitrogen-doped expanded graphite for high-performance sodium-ion battery anodes

Kangsheng Huang [a,b,1], Shiqi Tian [a,1], Hai Xu [a], Chang Fang [a], Langyuan Wu [a], HaiJun Wang [a], Fuliang Liu [a], Wenjie He [b,*], Xiaogang Zhang [a,*]

[a] Jiangsu Key Laboratory of Electrochemical Energy Storage Technologies, College of Materials Science and Engineering, Nanjing University of Aeronautics and Astronautics, Nanjing 210016, China

[b] School of Materials Science and Engineering, Henan Polytechnic University, Jiaozuo 454003, China

ARTICLE INFO

Keywords:
Ultrafast synthesis
Expanded graphite
Rich defects
Nitrogen doping
Sodium ions batteries

ABSTRACT

Graphite materials have been highly successful as anode materials for lithium-ion batteries (LIBs), but they show limited performance in sodium-ion batteries (SIBs) due to the insufficient interlayer spacing, which restricts Na^+ insertion and diffusion. In this work, we report the rapid synthesis of expanded graphite (EG) via a high-temperature shock reduction method and enhance its sodium storage capacity through nitrogen doping (EGN). The ultrafast nonequilibrium thermal shock generates a defect-rich structure in EGN, expanding the interlayer distance to 0.44 nm while maintaining the layered ordered structure characteristic of graphite-like materials. Spectroscopic analysis and theoretical calculations indicate that the successful incorporation of nitrogen atoms into expanded graphite increases the active sites and enhances Na^+ adsorption capability. Consequently, SIBs with EGN anodes achieve a reversible specific capacity of 295 mA h g^{-1} at 0.1 A g^{-1}. This work presents a cost-effective and efficient method for EG synthesis, offering a new strategy for designing advanced sodium-ion anode materials.

1. Introduction

The urgent need for low-carbon and efficient energy solutions has prompted researchers to conduct extensive work aimed at developing secondary batteries that combine high performance with low cost [1–8]. Sodium resources have great potential advantages that are not limited by region and abundance. In addition, SIBs and LIBs have similar rocking chair-like working principles and similar production technologies [9–14]. Therefore, sodium-ion battery has received increasing attention from industry and academia in recent years. Unfortunately, compared with the mature lithium-ion anode materials, sodium-ion battery anode materials are still in the exploration stage of optimization screening [15–20].

Graphite, known for its high energy density and low cost, has been successfully used as an anode material for LIBs. However, it performs poorly in SIBs due to the larger ionic radius of Na^+ compared to Li^+ (0.102 nm vs 0.076 nm) [21–25]. To address the low Na^+ storage efficiency caused by the mismatch between graphite interlayer spacing and the Na^+ ionic radius, researchers have explored various strategies to optimize the structure of graphite materials [26,27]. For instance, ether-based electrolytes have been developed to enable rapid Na^+ storage through the co-intercalation of solvent molecules and Na^+ ions [28–30]. Another effective strategy is to enhance Na^+ intercalation by increasing the graphite interlayer spacing via heteroatom doping [31–38]. While both approaches have shown promising results, they still face challenges such as low capacity, complex processes, high costs, and limited application scenarios. Recently, researchers have employed graphite oxidation to synthesize EG, increasing the interlayer spacing and introducing defects to facilitate Na^+ intercalation [39–41]. For example, Wang et al. synthesized EG with an interlayer spacing of 0.43 nm via a two-step redox process, achieving a capacity of 284 mAh g^{-1} as an anode material for SIBs [42]. Li et al. prepared EG using Hummer's method followed by heat treatment and clarified the reaction mechanisms of sodiation and desodiation processes through in situ Raman spectroscopy [43]. Recently, Jun's group developed a sodium-ion anode with a defect-rich structure generated through mechanical activation of graphite [44].

* Corresponding authors.
E-mail addresses: wenjiehe@hpu.edu.cn (W. He), azhangxg@nuaa.edu.cn (X. Zhang).
[1] Kangsheng Huang and Shiqi Tian contributed equally to this work.

https://doi.org/10.1016/j.cej.2025.159326
Received 7 October 2024; Received in revised form 1 December 2024; Accepted 5 January 2025
Available online 6 January 2025
1385-8947/

Their findings indicate that increasing defect density and interlayer spacing significantly enhances the sodium storage performance of graphite [33,45,46]. Therefore, establishing a simple and scalable method to produce defect-rich graphite-derived materials with expanded interlayer spacing is crucial for advancing the development and application of SIBs.

Among various thermal treatment methods, high-temperature shock (HTS) is a low-carbon, efficient, and flexible heating technology characterized by rapid heating kinetics (~300 K·min^{-1}), making it suitable for electrode material synthesis [47–49]. Compared to traditional equilibrium heating, this non-equilibrium method is more conducive to defect formation and shows great potential for preparing SIB anode materials. Additionally, heteroatom doping disrupts the π-π conjugated system between graphite layers, introducing electronegative functional groups that enhance the adsorption energy of sodium ions and accelerate their deintercalation [50]. This not only improves the conductivity of EG but also creates more active sites, increasing the specific capacity. Thus, combining the HTS method with heteroatom doping offers a promising approach for fabricating high-performance, low-cost SIB anode materials.

Here, we developed a rapidly prepared EG anode material for SIBs using graphite oxide as raw material by combining these two strategies-(1) preparation of EG by HTS and (2) optimization of sodium ion adsorption energy by nitrogen atom doping. Electron microscopy characterization indicates that the synthesized EG retains a graphite-like layered ordered structure with an expanded interlayer spacing of 0.44 nm.This structure provides favorable conditions for the electrochemical insertion of Na^+. Electrochemical tests demonstrate that the nitrogen-doped expanded graphite (EGN) delivers a high reversible capacity of 322mAh g^{-1} at a current density of 0.05 A g^{-1} and retains a specific capacity of 115mAh g^{-1} at 1.0 A g^{-1} after 1000 cycles. In-situ X-ray diffraction (XRD) and ex-situ Raman analyses are used to monitor the microstructural changes during sodiation and desodiation. The EGN prepared in this study combines low-carbon, high-efficiency features, making it a highly promising anode material for future SIBs applications.

2. Results and discussion

Preparation and structural characterization of expand graphite. The heating rate and final temperature achieved by Joule heating are highly dependent on the choice of heating substrate. To address this, we first conducted a screening of potential substrates, including tungsten foil, graphite sheet, and carbon paper. Comparative analysis revealed that tungsten foil exhibited the fastest heating rate and reached a maximum temperature of 2200°C, while graphite sheet showed the slowest heating rate with a maximum temperature of only 400°C. Carbon paper demonstrated a moderate heating rate and achieved a maximum temperature of 950°C (Fig. S1). To prevent nitrogen source evaporation and excessive graphitization, carbon paper was selected as the heating substrate. EGN is synthesized within seconds using the HTS method, as illustrated in Fig. 1a. As seen in Fig. 1b, the HTS process consists of three stages: rapid heating, constant temperature holding, and fast cooling. The heating rate can reach an impressive 95 °C/s (950 °C in 10 s), with the entire synthesis taking only 154 s, highlighting the high efficiency of HTS. During the process, the carbon substrate emits a bright light, accompanied by heat and pressure due to the high current, as shown in Fig. 1c. The ultrafast thermal shock causes rapid decomposition and release of oxygen-containing groups from the carbon layers, breaking the van der Waals forces between graphite layers and resulting in the formation of expanded graphite [51,52]. Additionally, the non-equilibrium heating conditions favor the formation of defects and nitrogen atom doping (Fig. 1c). Scanning electron microscopy (SEM) reveals the morphology and microstructure of graphite oxide (GO) after thermal shock. The particle size of GO is approximately 5 μm (Fig. 1d,), exhibiting a block structure. After rapid high-temperature impact, GO undergoes exfoliation, forming a 3D network structure resembling stacked nanosheets (Fig. 1e), driven by the rapid gas evolution [53]. When nitrogen atoms are doped into EG, EGN displays a

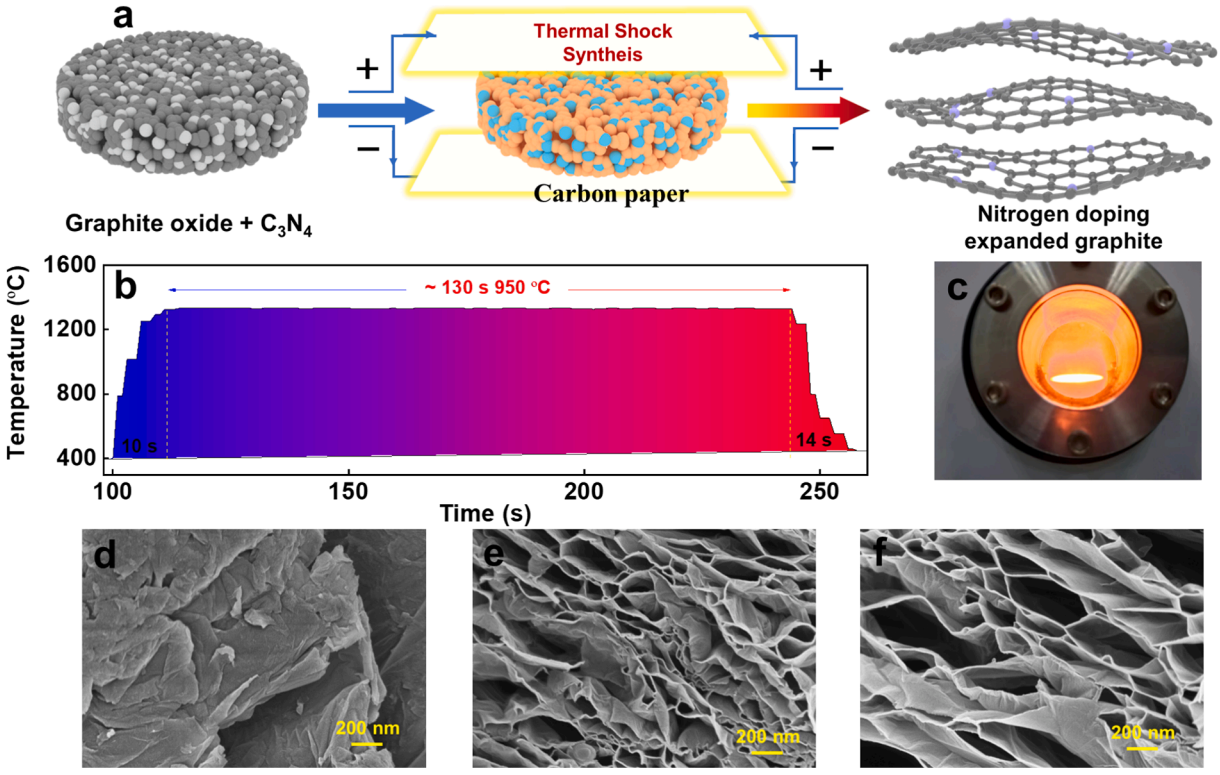

Fig. 1. (a) Schematic illustration of the process for preparing EGN by HTS; (b) Heating curve of HTS; (c) Digital photo of HTS process; (d-f) SEM images of GO, EG, EGN.

larger layered structure with more voids (Fig. 1f). At lower magnifications, the SEM images reveal that the GO undergoes uniform expansion after rapid thermal reduction, demonstrating excellent consistency (Fig. S2).

The above findings prove that the use of thermal shock can successfully achieve the rapid exfoliation of graphite oxide to form porous lamellar expanded graphite, and the whole process takes only 154 s.

The structure of EGN is further analyzed using high-resolution transmission electron microscopy (HRTEM). As shown in Fig. 2a, the top view of EGN reveals a well-defined lamellar film structure, while the cross-sectional view (Fig. 2b) shows an interlayer spacing of 0.44 nm, significantly larger than the 0.34 nm spacing typically found in graphite materials. The diffraction rings observed in the selected area electron diffraction (SAED) patterns further demonstrate that the EGN sample possesses a certain degree of ordered interlayer structure and crystallinity. To better observe the graphite-like layered ordered structure in EGN, we have provided additional TEM images, as shown in Fig. S3. To further investigate the bonding states of N, C, and O atoms in EGN, X-ray photoelectron spectroscopy (XPS) is performed (Fig. 2g-i). The full spectrum indicates a nitrogen doping level of 6.8 %, suggesting that N is successfully introduced through the thermal shock process (Fig. S1). The N1s XPS spectrum (Fig. 2g) shows three distinct peaks at 398 eV, 399 eV, and 400 eV, corresponding to pyridinic N, pyrrolic N, and graphitic N, respectively. Pyridinic nitrogen is the dominant species, and pyrrolic N has been reported to enhance cycling stability and electrochemical activity [54]. The C1s spectrum reveals four peaks at 284.6 eV, 285.5 eV, 288.5 eV, and 290.5 eV, which are attributed to C = C, C-O/C-N, C = O, and O-C = O bonds, respectively (Fig. 2e). A small amount of O is also present, primarily in the form of carbon oxides (Fig. 2f).

To investigate the changes in crystalline structure before and after thermal reduction, X-ray diffraction (XRD) is employed to characterize the GO, EG, and EGN samples. As shown in Fig. 2g, the commercial graphene oxide sample exhibits distinct peaks, particularly at 13°, indicating the presence of abundant oxygen-containing functional groups, and at 42°, reflecting disordered turbostratic carbon (disordered carbon layers with poor stacking and atomic defects) [55]. After thermal reduction, the characteristic peaks at these positions in EG and EGN nearly disappear, leaving only a diffraction peak at 21°, indicating an improvement in long-range order and the formation of a graphite-like structure with larger interlayer spacing. This observation aligns with the SEM and TEM characterization results.

Raman spectroscopy was further employed to analyze the degree of structural disorder at the local level in the samples. All three samples exhibit two characteristic Raman peaks: the D peak and the G peak, located at approximately 1348 cm^{-1} and 1597 cm^{-1}, respectively. The D peak is generally associated with defects in the carbon atomic structure, while the G peak corresponds to the in-plane stretching vibration of sp^2-hybridized carbon atoms. The intensity ratio of the D to G peaks (I_D/I_G) provides an indicator of the degree of microstructural defects within the carbon materials. The intensity ratios of the D band to the G band (I_D/I_G) for GO, EG, and EGN are 0.99, 1.02, and 1.03, respectively (Fig. 2h). The increase in the I_D/I_G ratio reflects the destruction of van der Waals forces between graphite oxide layers, resulting from the rapid decomposition and release of oxygen-containing groups, which leads to the expansion and exfoliation of the graphite layers. Nitrogen doping further enhances the defect density. Additionally, we observed a shift of the G peak to lower wavenumbers in GO after thermal reduction, indicating that the thermal reduction process effectively removed oxygen-containing

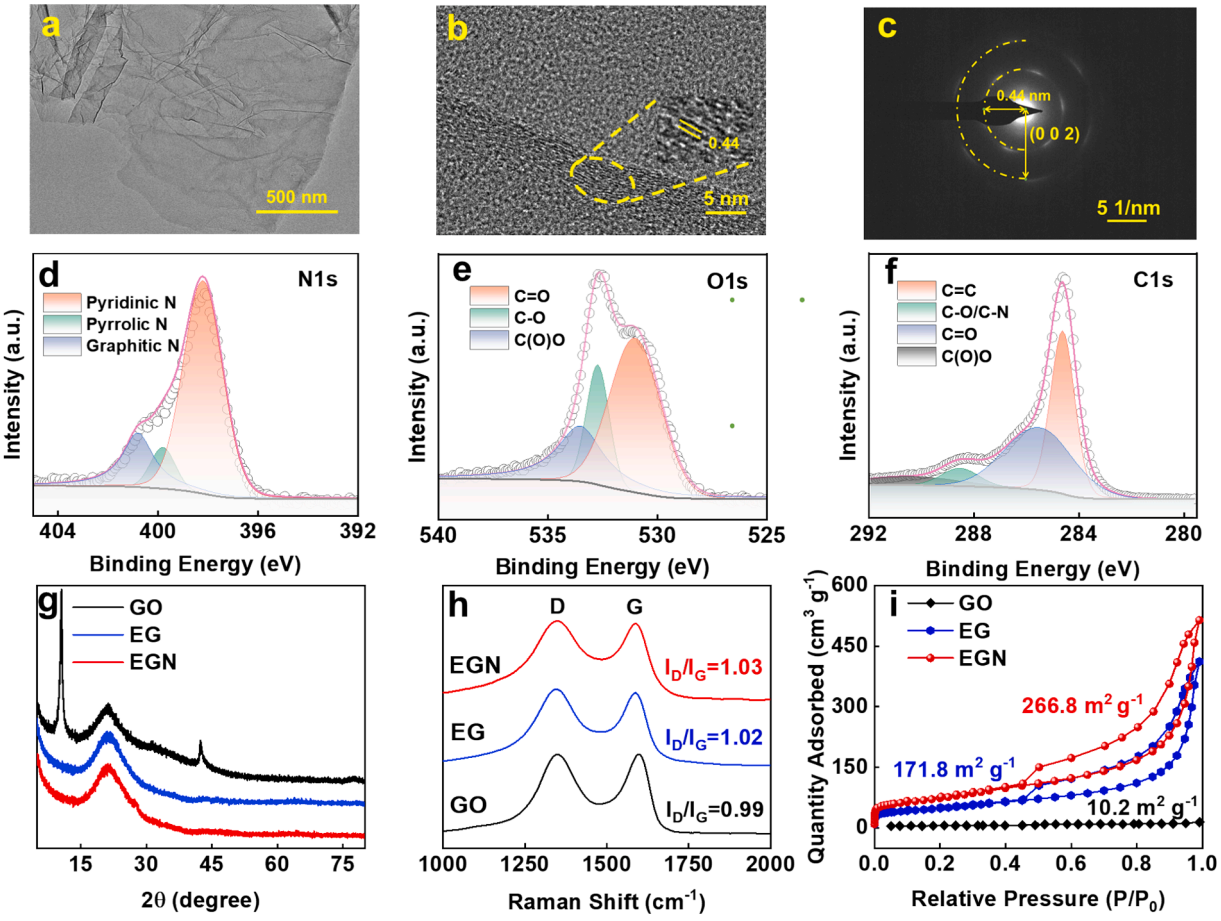

Fig. 2. (a) TEM images of EGN; (b) HRTEM images of EGN; (c) SAED patterns of EGN; (d) XRD patterns and (e) Raman spectra of GO, EG, and EGN; (f) N_2 adsorption and desorption isotherms of EGN, EG; High-resolution XPS spectra (g) N1s; (h) O1s; (i) C1s of EGN.

functional groups from graphite oxide. This removal promoted an increase in ordered layers, thereby enhancing the overall graphitic structure. This observation aligns well with the XRD results, further supporting our findings.

Moreover, BET analysis reveals significant differences in the pore structures of the materials. N_2 adsorption measurements at 77 K show that the surface area of the material increases substantially from GO to EG, rising from 12.0 m^2 g^{-1} to 171.8 m^2 g^{-1}, with EGN reaching 266.8 m^2 g^{-1} (Fig. 2i). The higher specific surface area and pore volume of EGN are attributed to fewer stacked layers and increased defect density, consistent with SEM and Raman results. The pore size distribution diagram for GO, EG, and EGN (Fig. S2) indicates that the materials primarily contain micropores and mesopores. The abundant mesopores may shorten ion diffusion paths, contributing to enhanced electrochemical ion storage performance. In summary, experimental characterizations confirm that the thermal shock method successfully synthesized nitrogen-doped, defect-rich expanded graphite with a graphite-like layered structure.

Performance of Sodium-ion cell. We evaluated the performance of Na-ion cells using GO, EG, and EGN samples as anodes. The initial electrochemical impedance spectroscopy (EIS) of the GO, EG, and EGN sodium-ion coin cells shows a short Warburg slope in the low-frequency region (0.1 Hz – 1.0 Hz) and a semicircle in the mid-to-high frequency range (100 mHz – 1.0 MHz)[56,57]. The high-frequency semicircle is attributed to the charge transfer process. The R_{ct} (charge transfer resistance) values for the three cells are 1343 Ω, 611.4 Ω, and 261.2 Ω, respectively, indicating that the increased interlayer spacing and nitrogen doping significantly reduce Na^+ migration resistance. At a current density of 0.1 A g^{-1}, the EGN cell exhibited a first-cycle reversible capacity of 295 mAh g^{-1} (Fig. S9a), which is notably higher than the 251 mAh g^{-1} and 236 mAh g^{-1} for the GO and EG cells. We observed that the initial Coulombic efficiency of the materials is relatively low (Fig. S9). This phenomenon primarily arises from side reactions between residual oxygen-containing functional groups, as well as the increased surface area following thermal reduction, which interact with the electrolyte. After 500 stable cycles, the EGN cell retained a capacity of 170.6 mAh g^{-1}, while the GO and EG cells showed similar capacities of around 120 mAh g^{-1} (Fig. 3a).

Fig. 3c illustrates the rate performance of GO, EG, and EGN at current densities ranging from 0.05 to 10 A g^{-1}. The EGN cell consistently outperformed the EG and GO cells at all current densities, achieving a maximum specific capacity of 322 mAh g^{-1} at 0.05 A g^{-1} (Fig. S4b). Even at a high current density of 10 A g^{-1}, the EGN cell delivered a charge capacity of 110 mAh g^{-1}, while the capacities of the other two cells dropped close to zero. Remarkably, when the current density is returned to 0.05 A g⁻1, the EGN cell's capacity is fully restored to its initial level. To examine the performance of the materials at low current density, we further tested the cycling stability of the three samples at 0.05 A g^{-1}. After 100 stable cycles, EGN retained a specific capacity of 216 mAh g^{-1}, whereas the GO-based battery only achieved 169 mAh

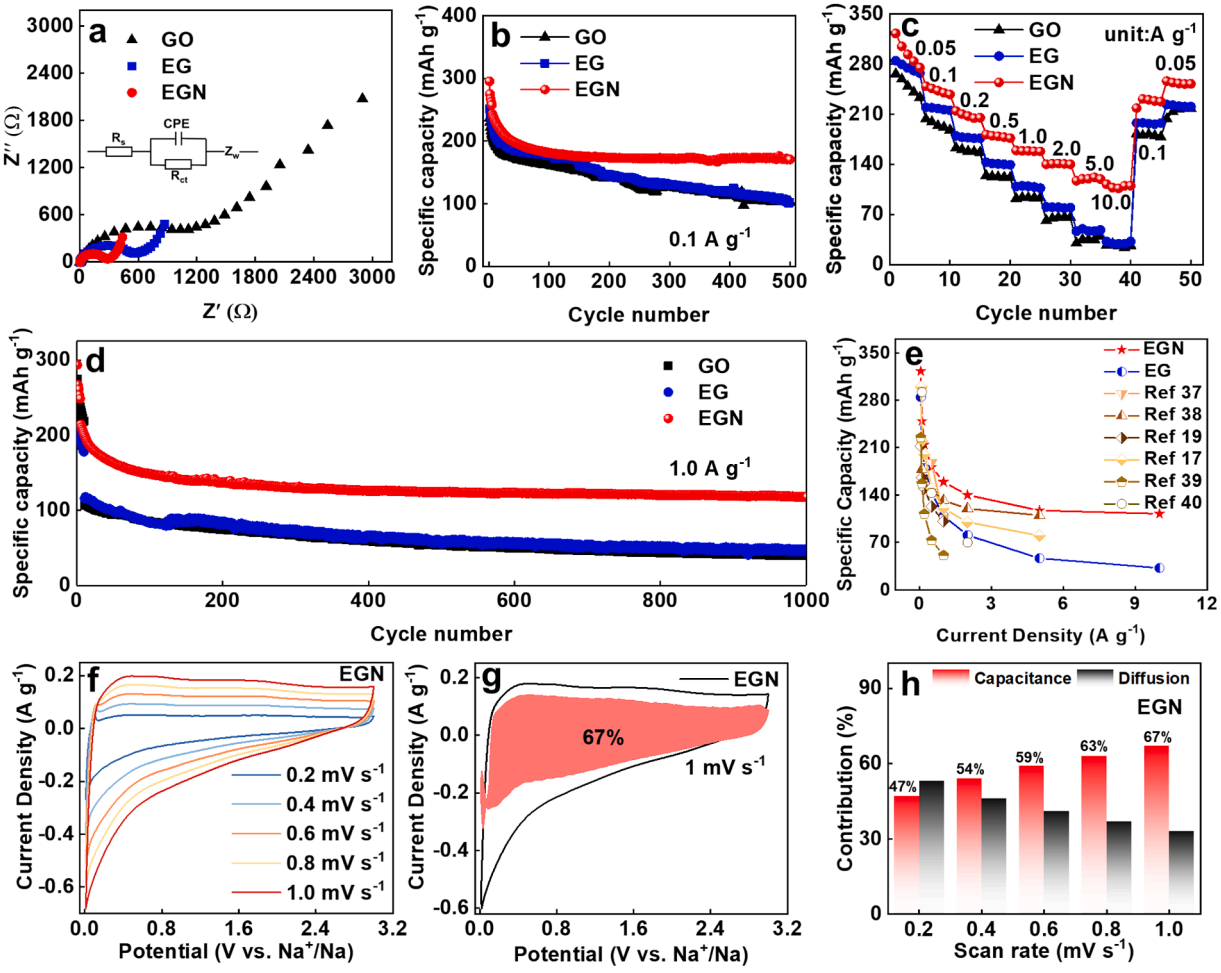

Fig. 3. (a) Electrochemical impedance spectroscopy results of sodium ion coin cells with GO, EG, and EGN anodes; Comparison of (a) cycling performance (0.1 A/g), (b) rate capability and (c) cycling performance at high current density (1.0 A/g) of GO, EG and EGN cells. (e) Comparative rate performance with the previously published typical carbon anode; (f) Separation of the capacitive and diffusion currents in EGN at 1 mV/s; (g) CV curves of EGN cell at different scan rates; (h) Ratio of the capacitive and diffusion-controlled charge's contribution to the scan rate.

g^{-1}. These results clearly demonstrate that N atom doping significantly enhances both the cycling stability and rate performance of expanded graphite.

Fig. 3d compares the capacities of EGN, EG, and GO cells at a high current density of 1.0 A g^{-1} over 1000 cycles. After 1000 cycles, the EGN cell maintained a capacity of 115 mAh g^{-1}, with a retention rate of 45 %, indicating exceptional cycling stability. Furthermore, Fig. 3e highlights the superior high-rate charge capacity of EGN compared to various other carbon materials reported in the literature, where EGN exhibits outstanding performance [43,58–62]. Given the excellent rate capacity and cycling stability of EGN at high current densities, it is both necessary and valuable to qualitatively and quantitatively assess the contributions of surface adsorption capacitance and diffusion-controlled intercalation processes to the cell's capacity. The contributions from internal diffusion intercalation or surface capacitance adsorption can be evaluated by calculating the current during the charge–discharge process.

Figs. 3f and S3 show the cyclic voltammetry (CV) curves of sodium-ion half-cells using EGN and EG materials at scan rates ranging from 0.2 to 1 mV s^{-1}. It is evident that the CV curve shape is well-maintained across the entire scan rate range. Using the equation $i = k_1\nu + k_2\nu^{\frac{1}{2}}$, which relates the scan rate (ν) to the current (i), the specific contributions of the two mechanisms—capacitive and diffusion-controlled processes—can be calculated [63]. In this equation,i and ν represent the current at a given voltage and the corresponding scan rate, while k_1 and k_2 are constants related to the voltage. The terms $k_1\nu$ and $k_2\nu^{1/2}$ represent the capacitive and diffusion-controlled contributions, respectively.

For instance, the shaded areas in Fig. 3g and Fig. S3 indicate the pseudocapacitance contributions of EGN and EG at a scan rate of 1.0 mV s^{-1}, which are 67 % and 63 %, respectively. The enhanced sodium storage kinetics of EGN primarily stem from the increased interlayer spacing and abundant defect structures formed through rapid thermal reduction [64,65]. We further analyzed the capacity contributions at different scan rates (Fig. 3h), and found that at lower scan rates, capacity is primarily controlled by diffusion. This is consistent with the CV curve at 0.1 mV s^{-1}, where an oxidation peak at 0.1 V (Fig. S4) indicates sodium ion intercalation into the layered structure. As the scan rate increases, the diffusion contribution decreases while the capacitive contribution rises correspondingly. Although a minor hump might appear due to the redox reaction, capacitive processes dominate across the entire potential range. Similarly, the EG anode material exhibits a comparable electrochemical reaction mechanism.

These results demonstrate that sodium-ion cells using EGN anodes exhibit excellent cycling stability and rate performance, suggesting significant potential for practical applications.

Sodium storage mechanism and structural evolution. To further investigate the underlying reasons for the excellent rate performance of the EGN cell, a kinetic analysis of the EGN electrodes is conducted. The sodium ion diffusion coefficient (D_{Na+}) for both EGN and EG electrodes

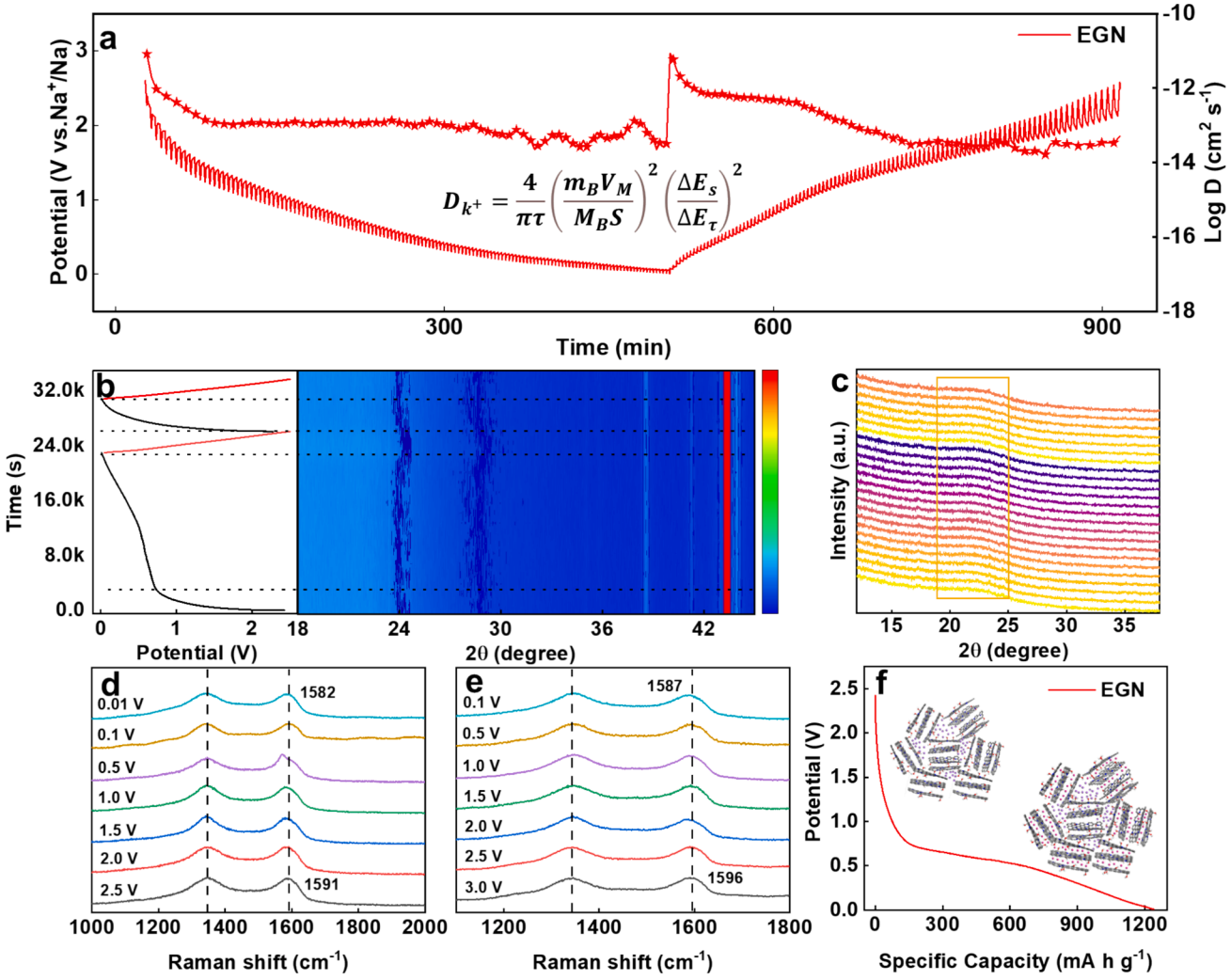

Fig. 4. (a) GITT curve of EGN cell and the corresponding logarithmic value of ion diffusion coefficient. (b, c) Time-resolved in situ XRD contour plots and spectra of the EGN cell in the first two cycles; (d, e) *Ex-situ* Raman spectra of EGN cell during the first charging/discharging process; (f) Discharge curves (0.1 A/g);

is first evaluated using the Galvanostatic Intermittent Titration Technique (GITT). Fig. 4**a** displays the potential response of the EGN electrode during the discharge/charge process, with the calculated D_{Na+} values ranging from 10^{-11} to 10^{-13} cm^2 s^{-1}. This enhanced efficiency is primarily attributed to the defect-rich structure and the larger interlayer spacing of EGN, which significantly lower the energy barrier for Na^+ diffusion, thereby improving the reaction kinetics.

The relationship between electrochemical behavior and structural evolution during cycling is further clarified using in-situ XRD tests. Fig. 4A presents contour plots showing the peak evolution of the EGN electrode, along with the cell voltage curve over time (left) (Fig. 4a.b). The (0 0 2) peak position of the EGN electrode exhibits regular shifts corresponding to the degree of sodiation and desodiation. Specifically, during the discharge process, the (0 0 2) peak shifts significantly to the left at lower potentials, then returns to its original position when recharged to OCV. This behavior confirms an "adsorption-insertion" mechanism during discharge and a gradual delamination during the entire charging process. The same peak shift pattern in 2θ is observed during the second charge and discharge cycle.

The structural evolution of the EGN anode during Na^+ insertion/extraction is further confirmed by ex situ Raman spectroscopy. During discharge, the G-band shifts from 1591 cm^{-1} to 1582 cm^{-1}, while the intensity of the D-band gradually decreases. This indicates that Na^+ insertion weakens the C-C bonds in the layered structure and Na^+ adsorption on defect sites and pores restricts the breathing vibration of sp^2 carbon rings. During the subsequent charging process, the G-band shifts back from 1588 cm^{-1} to 1591 cm^{-1}, as shown in Fig. 4e. These results suggest that the EGN sample, with its rich defect structure and expanded interlayer spacing while retaining a graphite-like layered ordered structure, follows a sodium storage mechanism where both adsorption and insertion coexist (Fig. 4f).

To further reveal the intrinsic reasons for the superior sodium-ion storage capacity, density functional theory (DFT) calculations are performed to explore the effects of N-doping and defect-rich structure on the electronic structure and sodium adsorption behavior. The most stable structure of the sodium ion adsorption system is optimized (Fig. 5a-c), where the Na absorption energy of EG is −1.48 eV, indicating that the interaction between Na and EG is weak. EG (−2.65 eV) exhibited a higher Na absorption energy than GO, indicating that the defect-rich structure played an active role in both Na adsorption and storage. In particular, the EGN model (−3.08 eV) exhibited the highest Na absorption energy among all samples, indicating that N-doping and defect structure can synergistically enhance the sodium absorption capacity (Fig. S11). The preparation of EGN with N-doping and defect-rich structure by nonequilibrium heating improved the electronic conductivity and reaction kinetics, resulting in excellent sodium storage

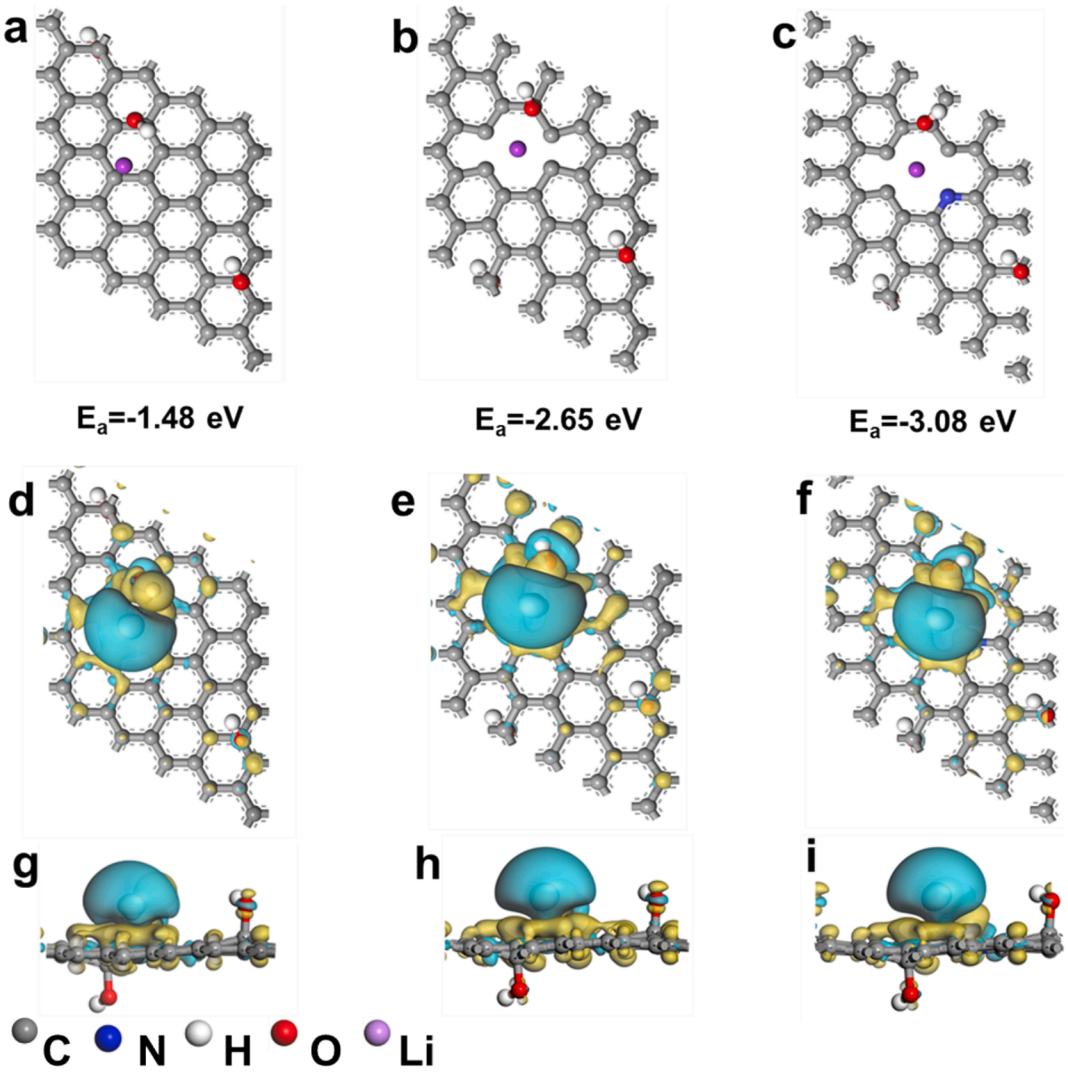

Fig. 5. DFT calculations are performed on the Na-adsorption models of (a) GO, (b) EG, and (c) EGN, respectively. Top (upper) and side (lower) views of the differential charge density plots of (d,g) GO, (e,h) EG, and (f,i) EGN for interaction with Na atoms.

capacity. To further explore the electronic structure and bonding characteristics of the Na intercalation process, the top and plan views of the charge density difference (red and blue correspond to negative and positive charge differences) are shown in Fig. 5d–i. Obviously, the electron-rich regions (yellow) prefer to gather around defects and N atoms, which is beneficial for capturing Na^+. The rich defect and N configurations synergistically regulate the spatial charge redistribution and increase the active host sites, significantly improving the electrosorption ability.

3. Conclusion

In summary, the high-temperature shock reduction method successfully produced defect-rich, nitrogen-doped EGN with an interlayer spacing of up to 0.44 nm while preserving the graphite-like layered ordered structure. The EGN anode, characterized by a high concentration of pyridinic nitrogen, abundant structural defects, and expanded interlayer spacing, demonstrates exceptional specific capacity alongside outstanding electrochemical kinetics. Accordingly, the SIBs equipped with the EGN anode delivers a reversible specific capacity of 295 mA h g^{-1} at 0.1 A g^{-1}., and even sustains a notable specific capacity of 115 mAh g^{-1} at a high current density of 10 A g^{-1}. Furthermore, in-situ XRD and ex-situ Raman analyses reveal that EGN exhibits a combined "adsorption-insertion" sodium storage mechanism during charge and discharge processes. This study highlights the potential of high-temperature shock technology as a low-carbon, efficient method for preparing expanded graphite, expanding the application prospects of graphite-based anodes in sodium-ion batteries.

CRediT authorship contribution statement

Kangsheng Huang: Writing – original draft, Methodology, Data curation. **Shiqi Tian:** Writing – original draft, Methodology, Data curation. **Hai Xu:** Investigation, Formal analysis, Data curation. **Chang Fang:** Investigation, Data curation. **Langyuan Wu:** Visualization, Formal analysis. **HaiJun Wang:** Investigation, Methodology. **Fuliang Liu:** Investigation, Methodology. **Wenjie He:** Writing – review & editing. **Xiaogang Zhang:** Writing – review & editing, Supervision, Funding acquisition, Conceptualization.

Declaration of competing interest

The authors declare that they have no known competing financial interests or personal relationships that could have appeared to influence the work reported in this paper.

Acknowledgements

Acknowledge the funding support from the National Key Research and Development Project Intergovernmental International Science and Technology Innovation Cooperation (2022YFE0109400), Leading Edge Technology of Jiangsu Province (BK20202008), National Natural Science Foundation of China (52372199) and Project Funded by the Priority Academic Program Development of Jiangsu Higher Education Institutions (PAPD). Thanks to Nanjing University of Aeronautics and Astronautics Analysis Test Center

Appendix A. Supplementary data

Supplementary data to this article can be found online at https://doi.org/10.1016/j.cej.2025.159326.

Data availability

Data will be made available on request.

References

[1] J.-Y. Hwang, S.-T. Myung, Y.-K. Sun, Chem. Soc. Rev. 46 (2017) 3529–3614.
[2] Y. Zhao, Y. Kang, J. Wozny, J. Lu, H. Du, C. Li, T. Li, F. Kang, N. Tavajohi, B. Li, Nat. Rev. Mater. 8 (2023) 623–634.
[3] L. Zhang, X. Li, M. Yang, W. Chen, Energy Storage Mater. 41 (2021) 522–545.
[4] Y. Jin, P.M. Le, P. Gao, Y. Xu, B. Xiao, M.H. Engelhard, X. Cao, T.D. Vo, J. Hu, L. Zhong, Nat. Energy 7 (2022) 718–725.
[5] Q. Wang, D. Zhou, C. Zhao, J. Wang, H. Guo, L. Wang, Z. Yao, D. Wong, G. Schuck, X. Bai, Nat. Sustainability 7 (2024) 338–347.
[6] Y. Yang, C. Wu, X.X. He, J. Zhao, Z. Yang, L. Li, X. Wu, L. Li, S.L. Chou, Adv. Funct. Mater. 34 (2024) 2302277.
[7] Y. Wan, B. Huang, W. Liu, D. Chao, Y. Wang, W. Li, Adv. Mater. (2024) 2404574.
[8] K. Sada, J. Darga, A. Manthiram, Adv. Energy Mater. 13 (2023) 2302321.
[9] Y. Wang, X. Xu, Y. Wu, F. Li, W. Fan, Y. Wu, S. Ji, J. Zhao, J. Liu, Y. Huo, Adv. Energy Mater. 14 (2024) 2401833.
[10] L. Chen, M. Chen, Q. Meng, J. Zhang, G. Feng, X. Ai, Y. Cao, Z. Chen, Angew. Chem. (2024) e202407717.
[11] C. Wu, Y. Yang, Y. Zhang, H. Xu, X. He, X. Wu, S. Chou, Chem. Sci. 15 (2024) 6244–6268.
[12] Y. Tang, Q. Zhang, W. Zuo, S. Zhou, G. Zeng, B. Zhang, H. Zhang, Z. Huang, L. Zheng, J. Xu, Nat. Sustainability 7 (2024) 348–359.
[13] H.S. Hirsh, Y. Li, D.H. Tan, M. Zhang, E. Zhao, Y.S. Meng, Adv. Energy Mater. 10 (2020) 2001274.
[14] Z. Li, Y. Zhang, J. Zhang, Y. Cao, J. Chen, H. Liu, Y. Wang, Angew. Chem. Int. Ed. 61 (2022) e202116930.
[15] S. Qiao, Q. Zhou, M. Ma, H.K. Liu, S.X. Dou, S. Chong, ACS Nano 17 (2023) 11220–11252.
[16] Z. Xu, J. Wang, Z. Guo, F. Xie, H. Liu, H. Yadegari, M. Tebyetekerwa, M.P. Ryan, Y. S. Hu, M.M. Titirici, Adv. Energy Mater. 12 (2022) 2200208.
[17] T. Zhang, C. Li, F. Wang, A. Noori, M.F. Mousavi, X. Xia, Y. Zhang, Chem. Rec. 22 (2022) e202200083.
[18] T. Zhang, F. Ran, Adv. Funct. Mater. 31 (2021) 2010041.
[19] R. Shao, Z. Sun, L. Wang, J. Pan, L. Yi, Y. Zhang, J. Han, Z. Yao, J. Li, Z. Wen, Angew. Chem. 136 (2024) e202320183.
[20] Y. Sun, R. Hou, S. Xu, H. Zhou, S. Guo, Angew. Chem. Int. Ed. 63 (2024) e202318960.
[21] Z. Zhang, Y. Chen, S. Sun, K. Sun, H. Sun, H. Li, Y. Yang, M. Zhang, W. Li, S. Chou, J. Mater. Sci. Technol. 119 (2022) 167–181.
[22] X. Zhang, C. Shen, H. Wu, Y. Han, X. Wu, W. Ding, L. Ni, G. Diao, M. Chen, Energy Storage Mater. 26 (2020) 457–464.
[23] A.N. Singh, M. Islam, A. Meena, M. Faizan, D. Han, C. Bathula, A. Hajibabaei, R. Anand, K.W. Nam, Adv. Funct. Mater. 33 (2023) 2304617.
[24] Y. Huang, X. Zhong, X. Hu, Y. Li, K. Wang, H. Tu, W. Deng, G. Zou, H. Hou, X. Ji, Adv. Funct. Mater. 34 (2024) 2308392.
[25] L. Lu, G. Guan, J. Wang, W. Meng, S. Li, Y. Zhang, F. Guo, Chem. Eng. J. 480 (2024) 147999.
[26] M. Qin, C. Chen, B. Zhang, J. Yan, J. Qiu, Adv. Mater. (2024) 2407570.
[27] K.C. Wasalathilake, H. Li, L. Xu, C. Yan, Journal of Energy Chemistry 42 (2020) 91–107.
[28] M.-Y. Sun, F.-D. Yu, Y. Xia, L. Deng, Y.-S. Jiang, L.-F. Que, L. Zhao, Z.-B. Wang, Chem. Eng. J. 430 (2022) 132750.
[29] M. Liu, L. Xing, K. Xu, H. Zhou, J. Lan, C. Wang, W. Li, Energy Storage Mater. 26 (2020) 32–39.
[30] Y. Wang, X. Wang, B. Zhao, Z. Ren, Z. Yao, W. Wei, J. Wang, J. Qin, J. Xie, M. Cao, Nano Energy 120 (2024) 109163.
[31] Y. Li, M. Chen, B. Liu, Y. Zhang, X. Liang, X. Xia, Adv. Energy Mater. 10 (2020) 2000927.
[32] Y. Yuan, Z. Chen, H. Yu, X. Zhang, T. Liu, M. Xia, R. Zheng, M. Shui, J. Shu, Energy Storage Mater. 32 (2020) 65–90.
[33] X. Hu, Y. Ma, W. Qu, J. Qian, Y. Li, Y. Chen, A. Zhou, H. Wang, F. Zhang, Z. Hu, Angew. Chem. 135 (2023) e202307083.
[34] Y. Jin, S. Wu, Y. Wang, Z. Xu, L. Chen, H. Yang, J. Storage Mater. 100 (2024) 113682.
[35] L. Li, M. Sun, Z. Xu, Z. Wang, K. Liu, Y. Chen, Z. Wang, H. Chen, H. Yang, Colloids Surf. A Physicochem. Eng. Asp 661 (2023) 130927.
[36] X. Zou, C. Dong, Y. Jin, D. Wang, L. Li, S. Wu, Z. Xu, Y. Chen, Z. Li, H. Yang, Colloids Surf. A Physicochem. Eng. Asp 672 (2023) 131715.
[37] Y. Li, X. Zou, S. Li, Y. Chen, G. Wang, H. Yang, H. Tian, J. Mater. Chem. A 2024 (12) (2024) 18324–18337.
[38] S. Wu, Y. Jin, D. Wang, Z. Xu, L. Li, X. Zou, M. Zhang, Z. Wang, H. Yang, J. Storage Mater. 68 (2023) 107731.
[39] H. Zhang, Y. Yang, D. Ren, L. Wang, X. He, Energy Storage Mater. 36 (2021) 147–170.
[40] L. Zhao, B. Ding, X.Y. Qin, Z. Wang, W. Lv, Y.B. He, Q.H. Yang, F. Kang, Adv. Mater. 34 (2022) 2106704.
[41] X. Fan, X. Kong, P. Zhang, J. Wang, Energy Storage Mater. 69 (2024) 103386.
[42] Y. Wen, K. He, Y. Zhu, F. Han, Y. Xu, I. Matsuda, Y. Ishii, J. Cumings, C. Wang, Nat. Commun. 5 (2014) 4033.
[43] X. Li, Z. Liu, J. Li, H. Lei, W. Zhuo, W. Qin, X. Cai, K.N. Hui, L. Pan, W. Mai, Journal of Energy Chemistry 53 (2021) 56–62.
[44] S.C. Lee, Y.H. Kim, J.H. Park, D. Susanto, J.Y. Kim, J. Han, S.C. Jun, K.Y. Chung, Adv. Sci. (2024) 2401022.
[45] C. Cai, Y. Chen, P. Hu, T. Zhu, X. Li, Q. Yu, L. Zhou, X. Yang, L. Mai, Small 18 (2022) 2105303.

[46] H. Huang, R. Xu, Y. Feng, S. Zeng, Y. Jiang, H. Wang, W. Luo, Y. Yu, Adv. Mater. 32 (2020) 1904320.
[47] C. Wang, W. Ping, Q. Bai, H. Cui, R. Hensleigh, R. Wang, A.H. Brozena, Z. Xu, J. Dai, Y. Pei, Science 368 (2020) 521–526.
[48] J. Liu, Y. You, L. Huang, Q. Zheng, Z. Sun, K. Fang, L. Sha, M. Liu, X. Zhan, J. Zhao, Adv. Mater. (2024) 2407369.
[49] P. Huang, Z. Li, L. Chen, Y. Li, Z. Liu, J. Zhang, J. Luo, W. Zhang, W.-D. Liu, X. Zhang, ACS Nano 18 (2024) 18344–18354.
[50] M. Liang, Y. Ren, J. Cui, X. Zhang, S. Xing, J. Lei, M. He, H. Xie, L. Deng, F. Yu, Nat. Commun. 15 (2024) 6437.
[51] Q. Wei, L. Xu, Z. Tang, Z. Xu, C. Xie, L. Guo, W. Li, J. Ind. Eng. Chem. 122 (2023) 562–572.
[52] D.-K. Son, J. Kim, M.R. Raj, G. Lee, Carbon 175 (2021) 187–201.
[53] J. Chen, Z. Mao, L. Zhang, D. Wang, R. Xu, L. Bie, B.D. Fahlman, ACS Nano 11 (2017) 12650–12657.
[54] X. Mou, J. Ma, S. Zheng, X. Chen, F. Krumeich, R. Hauert, R. Lin, Z.S. Wu, Y. Ding, Adv. Funct. Mater. 31 (2021) 2006076.
[55] V. Nebol'Sin, V. Galstyan, Y. Silina, Surf. Interfaces 21 (2020) 100763.
[56] Z. Chen, X. Lu, Y. Zhang, Y. Kang, X. Jin, X. Zhang, Y. Li, H. Wang, W. Huang, Adv. Funct. Mater. 34 (2024) 2314176.
[57] W. Huang, S. Wang, X. Zhang, Y. Kang, H. Zhang, N. Deng, Y. Liang, H. Pang, Adv. Mater. 35 (2023) 2310147.
[58] H. Chen, N. Sun, Y. Wang, R.A. Soomro, B. Xu, Energy Storage Mater. 56 (2023) 532–541.
[59] C. Chen, Z. Wang, B. Zhang, L. Miao, J. Cai, L. Peng, Y. Huang, J. Jiang, Y. Huang, L. Zhang, Energy Storage Mater. 8 (2017) 161–168.
[60] Y. Tang, X. Wang, J. Chen, X. Wang, D. Wang, Z. Mao, Carbon 174 (2021) 98–109.
[61] Y. Sun, J. Tang, K. Zhang, J. Yuan, J. Li, D.-M. Zhu, K. Ozawa, L.-C. Qin, Nanoscale 9 (2017) 2585–2595.
[62] Z. Tang, S. Zhou, P. Wu, H. Wang, Y. Huang, Y. Zhang, D. Sun, Y. Tang, H. Wang, Chem. Eng. J. 441 (2022) 135899.
[63] J. Yang, Z. Ju, Y. Jiang, Z. Xing, B. Xi, J. Feng, S. Xiong, Adv. Mater. 30 (2018) 1700104.
[64] P. Li, Y. Shen, X. Li, W. Huang, X. Lu, Energy Environ. Mater. 5 (2022) 608–616.
[65] W.-H. Huang, Z. Chen, H.-Y. Wang, L. Wang, H.-B. Zhang, H. Wang, Chem. Commun. 58 (2022) 4496–4499.